IEEE Access
Multidisciplinary | Rapid Review | Open Access Journal

IEEE MAGNETICS SOCIETY SECTION

Received 12 December 2023, accepted 18 December 2023, date of publication 22 December 2023,
date of current version 10 January 2024.

Digital Object Identifier 10.1109/ACCESS.2023.3346322

METHODS

Transformer Design Technique Based on the Magnetic Equivalent Model of High-Frequency Isolated LLC Converter With High Accuracy and Reduced Design Time

HAE-CHAN PARK[1], JONG-UK YANG[1,2], JIN-SU JANG[1], AND RAE-YOUNG KIM[1], (Senior Member, IEEE)
[1]Department of Electrical and Biomedical Engineering, Hanyang University, Seoul 04763, South Korea
[2]Power Electronics Research and Development Laboratory, LG Electronics, Seoul 08517, South Korea

Corresponding author: Rae-Young Kim (rykim@hanyang.ac.kr)

This work was supported by the Korea Institute of Energy Technology Evaluation and Planning (KETEP) Grant funded by the Korean Government Ministry of Trade, Industry and Energy (Development of High Efficiency Power Converter Based on Multidisciplinary Design and Optimization Platform) under Grant 2018201010650A and Grant 20212020800020.

ABSTRACT High-frequency isolated LLC converters, which require both high efficiency and high density, are gaining important as pivotal technological challenges. In these converters, the transformer plays an essential role not only in providing galvanic isolation between the input and output and in facilitating voltage step-up and step-down but also as a key component in resonance. An appropriate design of the transformer size and structure is required to achieve both high efficiency and high density. This study introduces a self-equivalent magnetic model that incorporates the fringing effect, presenting a design methodology that utilizes this model. Compared with traditional transformer design methods, the proposed methodology allows for a more precise design by considering both the relative permeability and the magnetic path length (MPL), which represents the average path of the magnetic flux. In addition, we employ pareto optimal design techniques to extract a pareto set of transformer designs that satisfy specific conditions and, apply weighting factors to propose an optimal design. The feasibility of the proposed optimal transformer design methodology was verified through finite element analysis simulations and empirical tests using LLC converters.

INDEX TERMS High efficiency, high power density, high frequency, high frequency transformer, LLC converter, Pareto optimal design method, reluctance modeling, shell-type transformer, wire winding.

I. INTRODUCTION

LLC resonant converters have seen a rapid increase in applications across various industries, such as electric vehicle chargers, power converters for fuel cells, server modules, and photovoltaic (PV) systems caused by their advantages of achieving high efficiency through zero-voltage switching (ZVS) and zero-current switching (ZCS), as well as excellent output voltage control characteristics under light-load conditions [1], [2], [3]. High-frequency transformers often employ a magnetizing inductance with air gaps added within the transformer core for preventing core saturation to achieve resonance at a lower cost or higher density [4]. However, when the size of the air gap becomes relatively large compared with that of the core, the fringing effect, which causes magnetic leakage at the sides of the air gaps, increases, reducing the accuracy of predicting the magnetizing inductance of the transformer.

Various magnetic-equivalent model analysis methods based on Rowland's law [5], [6] have been proposed to accurately predict the magnetizing inductance of transformers [7], [8], [9], [10], [11], [12], [13]. In [7], the optimal point

The associate editor coordinating the review of this manuscript and approving it for publication was Montserrat Rivas.

was found from a loss perspective by calculating the copper loss and iron loss of the transformer. This approach was applied to transformer topologies without air gaps, thereby neglecting the fringing effect. However, this method faces limitations when applied to topologies requiring air gaps in transformers, as it results in inaccurate predictions of inductance. References [8], [9], and [10] proposed wire-winding techniques for designing high-frequency transformers and presented the results of loss analysis and temperature prediction. However, these methods do not consider leakage inductance or the fringing effect, lowering the prediction accuracy. References [11], [12], and [13] presented improved magnetic-equivalent models that account for leakage inductance and the fringing effect, achieving relatively high predictive accuracy but at the cost of computational complexity and long execution times. Moreover, these methods are shape- and winding-dependent, limiting their applicability to various transformer designs.

However, active research is conducted on transformer design techniques that apply optimization algorithms based on magnetic-equivalent model analysis methods [14], [15]. Reference [14] proposed a technique applying the nondominated sorting genetic algorithm (NSGA), which iteratively refines multiple solutions for eventually finding an optimal solution, although it can be time-consuming. Reference [15] proposed an automatic transformer design technique using the whale optimization algorithm (WOA), which converges quickly because of fewer parameters but may depend on the initial guess of the optimal point, affecting its optimization performance.

Herein, a high-frequency transformer design technique that applies multi-objective optimization algorithm (MOA) based on an improved magnetizing inductance prediction model to enhance predictive accuracy and reduce design time is proposed. The improved magnetizing inductance prediction model introduces a curved magnetic flux path model for analyzing the exact magnetic flux path and simultaneously considering the permeability of the ferrite core to increase predictive accuracy. Moreover, we achieved a fast search speed and stable optimization performance by adopting MOA optimization techniques that utilize utopia point as the initial optimal point for search. The validity of the proposed high-frequency transformer design technique was verified through finite element analysis and experiments using a 500 W LLC resonant converter.

II. TRANSFORMER LOSS

Transformer losses are divided into winding and core losses because this study focuses on the design of high-frequency transformers using Litz wire, and it is assumed that AC losses have minimal impact.

A. WINDING LOSS

Winding losses in transformers occur when current flows through the transformer windings. These losses are proportional to the square of the current and the internal resistance of the transformer winding. The primary and secondary currents differ because of the turns ratio of the transformer, necessitating different winding wire thicknesses. Therefore, the winding losses for the primary and secondary sides are calculated individually and then summed. The winding resistance for both the primary and secondary sides is expressed as follows:

$$R_p = \sigma \frac{l_{winding\_pri}}{A_{pri}}, R_s = \sigma \frac{l_{winding\_sec}}{A_{sec}} \tag{1}$$

where σ represents the conductivity of copper, $l_{winding\_pri}$ and $l_{winding\_sec}$ represent the lengths of the primary and secondary windings, respectively, and A_{pri} and A_{sec} represent their respective cross-sectional areas.

The total winding losses on both the primary and secondary sides are expressed as follows:

$$P_{winding} = I_{p,rms}^2 R_p + I_{s,rms}^2 R_s \tag{2}$$

B. CORE LOSS

Core losses in transformers are losses incurred within the transformer core, primarily owing to magnetic induction. These losses are influenced by various factors related to the relative permeability of the core material, shape of the core, and magnetic properties. Several approaches exist for calculating core losses using hysteresis models, loss separation approaches, and empirical methods [16].

The hysteresis model is based on methods such as the Jiles–Atherton or Preisach models and focuses on the calculation of electronic energy [17], [18]. The loss separation approach measures three losses: hysteresis, eddy current, and magnetization losses [19], [20].

Both the hysteresis and loss-separation methods offer a high degree of accuracy, albeit at the cost of requiring comprehensive calculations or measurements. By contrast, the empirical approach proves to be user friendly because it capitalizes on the manufacturer-supplied data. The traditional Steinmetz equation provides a framework for characterizing the magnetic loss density across a range of loss curves. However, this equation, which is fundamentally rooted in sinusoidal waveform data, falls short in terms of accuracy when applied to nonsinusoidal waveforms under which substantially greater losses are measured. Several modified equations have been proposed to rectify this discrepancy for nonsinusoidal applications, which includes the modified Steinmetz equation (MSE), general Steinmetz equation (GSE), and improved general Steinmetz equation (IGSE) [21], [22].

The MSE was initially introduced to account for nonsinusoidal waveforms, demonstrating high accuracy by associating the rate of change in magnetic induction with core losses. Although the MSE has been validated for nonsinusoidal waveforms, it has not been verified for sinusoidal waveforms. To address this, the GSE was introduced, which considers not only the rate of change in magnetic induction but also the instantaneous values of the magnetic flux density. However, the response of the core material to specific

magnetic fluctuations varies depending on the dataset used. To overcome this issue, the IGSE was introduced by replacing the instantaneous values of magnetic induction with peak-to-peak values. This approach incorporates not only differential and instantaneous values but also the time history of the core material.

In this study, the IGSE method is used to calculate core losses. The core loss per unit volume using the IGSE approach is expressed as follows:

$$P_{core} = \frac{1}{T}\int_0^T k_i \left|\frac{dB(t)}{dt}\right|^{\alpha} \Delta B^{\beta-\alpha} dt \tag{3}$$

where α, β, and K denote the material coefficients of the core and T represents the period. Further, k_i is expressed as follows:

$$\begin{aligned} k_i &= \frac{K}{2^{\beta-1}\pi^{\alpha-1}\int_0^{2\pi}|\cos\theta|^{\alpha}\,d\theta} \\ &= \frac{K}{2^{\beta-1}\pi^{\alpha-1}\left(1.1044 + \frac{6.8244}{\alpha+1.354}\right)} \end{aligned} \tag{4}$$

Upon substituting equation (4) into equation (3) and expanding the integral expression, the result (kW/m^3) can be represented as follows:

$$P_{core} = k_i \cdot f^{\alpha} \cdot \Delta B^{\beta} \cdot \left(D^{1-\alpha} + (1-D)^{1-\alpha}\right) \tag{5}$$

where, D denotes the duty cycle.

III. CONVENTIONAL RESEARCH REVIEW

A. MAGNETIC EQUIVALENT MODEL [8], [9], [10]

Fig. 1(a) shows the conventional magnetic path analysis model. The existing model considers the magnetic flux path to be orthogonal and calculates the reluctance to formulate a magnetic equivalent circuit, as shown in Fig. 1(b). Fig. 2(a) shows the cross-sectional area of the EE core, and Fig. 2(b) shows its length. Utilizing these, the cross-sectional area of the EE core can be calculated as represented by the following:

$$A_{\text{top}} = A_{\text{bot}} = w_b \cdot w_d \tag{6}$$

$$A_{\text{side1}} = A_{\text{side3}} = A_{\text{left gap}} = A_{\text{right gap}} = w_e \cdot w_d \tag{7}$$

$$A_{\text{side2}} = A_{\text{center gap}} = w_c \cdot w_d \tag{8}$$

$$L = \frac{N^2}{\Re} \tag{9}$$

$$\Re_{\text{top}} = \Re_{\text{bot}} = \frac{2w_s + w_e + w_c}{2\mu_r\mu_0 w_d w_b} \tag{10}$$

$$\Re_{\text{side1}} = \Re_{\text{side3}} = \frac{2w_a + w_b}{2\mu_r\mu_0 w_d w_b} \tag{11}$$

$$\Re_{\text{side2}} = \frac{2w_a + w_b}{2\mu_r\mu_0 w_d w_c} \tag{12}$$

$$\Re_{\text{left gap}} = \Re_{\text{right gap}} = \frac{l_g}{\mu_0 w_d w_e} \tag{13}$$

$$\Re_{\text{center gap}} = \frac{l_g}{\mu_0 w_d w_c} \tag{14}$$

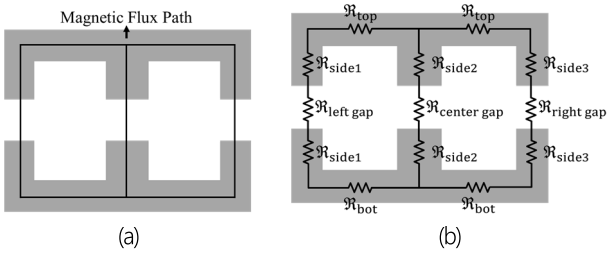

FIGURE 1. (a) Conventional magnetic flux path model. (b) Conventional magnetic equivalent model.

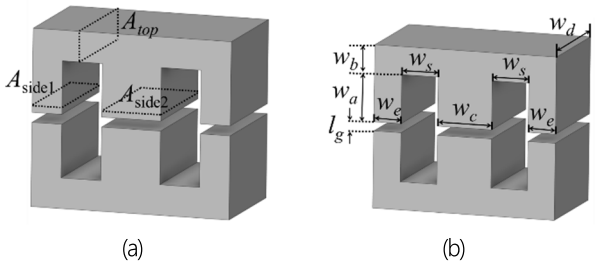

FIGURE 2. (a) Surface area of EE core. (b) length of EE core.

The inductance can be determined by substituting the reluctances calculated from Equations (10)–(14) into equation (9). However, the conventional magnetic equivalent model exhibits limitations in the prediction accuracy of inductance because the actual path of the magnetic flux does not follow a right angle but rather exhibits a curved trajectory. Fig. 3 shows the actual path of the magnetic flux obtained through finite element analysis simulations using the ANSYS Maxwell software. This suggests that incorporating a curved flux path model considers actual flux paths that can enhance the precision of the inductance predictions.

B. OPTIMIZATION TECHNIQUE BASED TRANSFORMER DESIGN METHOD

1) NSGA [14]

NSGA is a metaheuristic algorithm that mimics the evolutionary mechanisms found in nature and is employed to solve complex optimization problems. Fig. 4 shows an example of the NSGA execution.

First, a population is formed by encoding solutions to the problem at hand into a data structure composed of zeros and ones, known as the initial population.

Second, a subset of the initial population is randomly selected to form a mating pool.

Third, crossover operations were performed within the mating pool to mix and generate new solutions.

Finally, mutations were randomly introduced into the chromosomes to prevent stagnation and derive new solutions.

A limitation of this approach is that it is computationally expensive, particularly when the size of the mating pool, which signifies the number of iterations, is large.

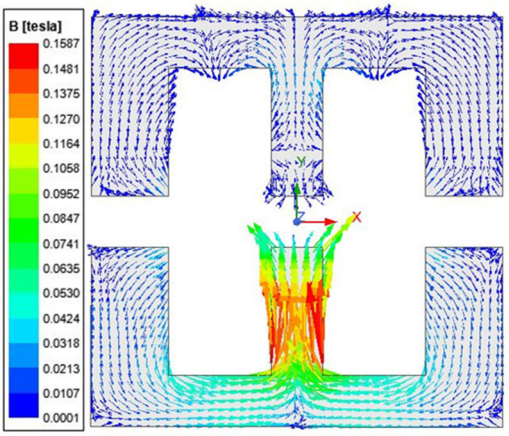

FIGURE 3. Actual magnetic flux path using Finite Element Analysis (FEA) simulation.

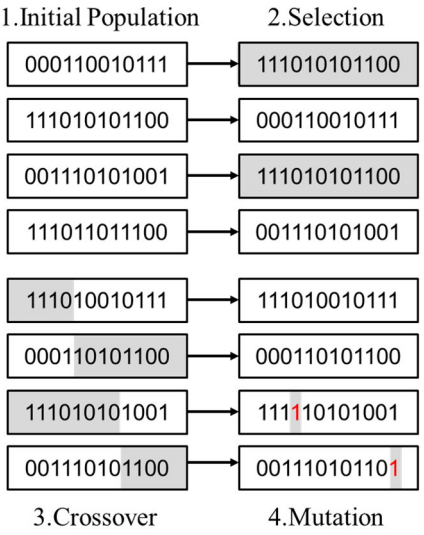

FIGURE 4. Example of using nondominated sorting genetic algorithm (NSGA).

Therefore, it is essential to set a sufficiently large mating pool; however, it is also important to acknowledge that the process of repeatedly performing crossovers and mutations can be time consuming.

2) WOA [15]

The WOA is a metaheuristic algorithm inspired by the foraging behavior of humpback whales, which involves a unique spiral movement pattern to encircle their prey. This spiral pattern is a critical aspect of the algorithm, as demonstrated in Fig. 5. Initially, the search agent (Whale) is randomly assigned a location (X, Y) to seek the optimal point (Prey). In the second phase, the initially assumed coordinates (X', Y') are considered the true optimal point, and the agent begins its search following a spiral trajectory, emulating the humpback whale's hunting strategy of gradually tightening circles around its prey. The final stage involves the agent iteratively adjusting its position in this spiral manner until reaching a predefined number of iterations, thereby pinpointing the optimal point. This technique, with its flexible and spiral search pattern, requires multiple iterations and tends to find solutions near the initially assumed optimal point. However, the optimization effectiveness of this approach is limited, as it heavily relies on the initial presumption of the optimal point's location.

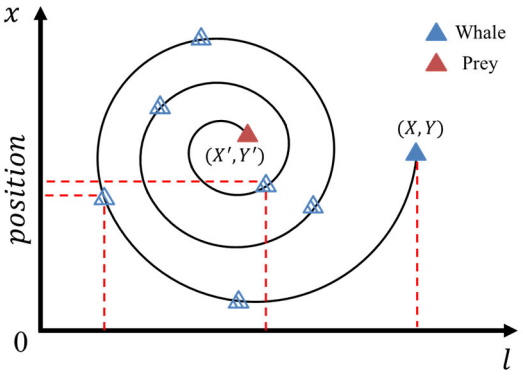

FIGURE 5. Example of using whale optimization algorithm (WOA).

IV. PROPOSED MAGNETIC EQUIVALENT MODEL

A. MAGNETIC EQUIVALENT MODEL CONSIDERING MAGNETIC PATH LENGTH

Fig. 1(a) shows a model of a curved magnetic path designed to overcome limitations inherent in traditional magnetic equivalent models by more accurately depicting the actual path of the magnetic flux. The application of these curved flux paths improves the precision of the magnetizing inductance predictions. Considering that the shape of the curved path can be either circular or elliptical, and the model was formulated to accommodate both scenarios depending on the type of EE core used.

Fig. 6(a), and Fig. 6(b) shows detailed illustrations of the flux paths for scenarios in which the corner shape is circular or elliptical. For commonly used EE cores such as E55/28/21, an elliptical equation must be employed to determine the flux path because the radii $w_b/2$ and $w_e/2$ differ. However, for special-purpose Planar EE cores such as E22/6/16/R, the radii $w_b/2$ and $w_e/2$ are equal, allowing the use of a circular equation. The perimeter of the ellipse can be calculated using $\pi\sqrt{2\left(r_1^2+r_2^2\right)}$, where $r_1 = w_b$ and $r_2 = w_e$. Therefore, the length of the curved corner, denoted by l_r, can be represented as one-fourth of the perimeter of the ellipse, as specified in the following:

$$l_r \approx \frac{\pi}{16}\sqrt{w_e^2 + w_b^2} \tag{15}$$

The circumference of a circle is $2\pi r$, where $r = w_b/2 = w_e/2$. Therefore, the length of the curved corner, denoted

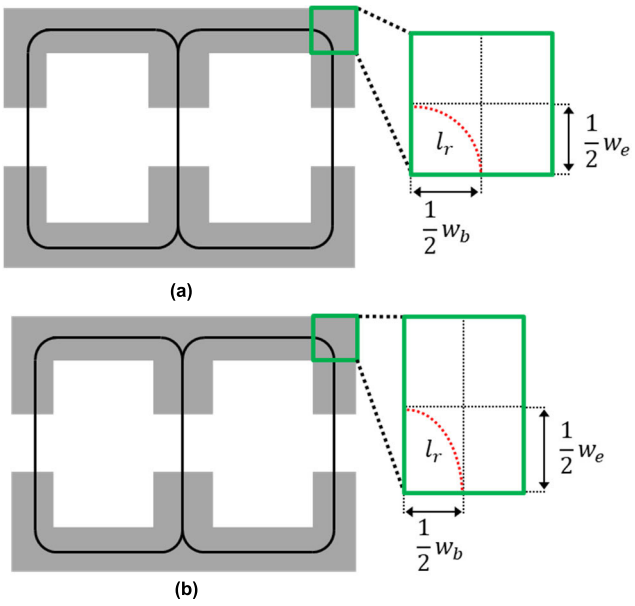

FIGURE 6. (a) Enlarged circle corner (b) Enlarged ellipse corner.

by l_r, can be represented as one-fourth of the circumference of the circle, as follows:

$$l_r = \frac{\pi w_b}{4} = \frac{\pi w_e}{4} \tag{16}$$

Utilizing the aforementioned methodology, the magnetic reluctance is derived through the application of equation (17), as elaborated in the following equations:

$$\Re = \frac{l}{\mu_r \mu_0 A} \tag{17}$$

$$\Re_{\text{top}} = \Re_{\text{bot}} = \frac{w_s + l_r}{\mu_r \mu_0 w_d w_b} \tag{18}$$

$$\Re_{\text{side1}} = \Re_{\text{side3}} = \frac{2w_a + l_r}{2\mu_r \mu_0 w_d w_b} \tag{19}$$

$$\Re_{\text{side2}} = \frac{w_a + l_r}{\mu_r \mu_0 w_d w_c} \tag{20}$$

$$\Re_{\text{left gap}} = \Re_{\text{right gap}} = \frac{l_g}{\mu_0 w_d w_e} \tag{21}$$

$$\Re_{\text{center gap}} = \frac{l_g}{\mu_0 w_d w_c} \tag{22}$$

The cross-sectional area of the core was determined based on equations (6)–(8).

B. MAGNETIC EQUIVALENT MODEL CONSIDERING FRINGING EFFECT

The error in inductance prediction becomes a significant concern in transformer design when the fringing effect is not considered. The fringing effect refers to the phenomenon where magnetic flux around the transformer core extends beyond the physical boundaries of the core into the surrounding space, directly impacting inductance calculations. When the fringing effect occurs around the transformer core, the total flux may not be accurately computed, leading to lower inductance values than the actual ones.

Failure to account for the fringing effect in inductance calculations can result in significant errors in transformer design, affecting performance and efficiency. These errors can potentially compromise transformer performance, especially in precision applications. Therefore, it is crucial to appropriately consider the fringing effect when designing transformers to accurately predict inductance values. This consideration is a fundamental element in ensuring the overall performance and reliability of transformers.

Fig. 7 shows the analysis model of the fringing effect in the EE core. Accurately calculating the fringing flux path is challenging, and therefore, the following assumptions were considered [23], [24], [25]

1) The fringing flux is composed of a combination of arcs and straight lines
2) The fringing flux occurs at up to half the length of the core leg.

The fringing flux can be calculated using integration techniques because of the presence of infinitely many fringing flux paths parallel to the specified path. Given that these flux paths are connected in parallel, the permeance is initially utilized to compute the fringing flux, followed by taking its reciprocal to determine the fringing reluctance. The fringing effect in terms of permeance is expressed by the following:

$$\begin{aligned} P_{\text{fring}} &= \int_0^{\frac{w_a}{2}} \frac{\mu_0 w_d}{l_g + \pi x} dx = \frac{\mu_0 w_d}{\pi} \int_0^{\frac{w_a}{2}} \frac{\pi}{l_g + \pi x} dx \\ &= \frac{\mu_0 w_d}{\pi} \left[ln\left(l_g + \frac{\pi w_a}{2}\right) - ln\left(l_g\right) \right] \\ &= \frac{\mu_0 w_d}{\pi} ln\left(1 + \frac{\pi w_a}{2 l_g}\right) \end{aligned} \tag{23}$$

where w_d denotes the core thickness. The fringing reluctance is given as follows:

$$\Re_{\text{fring}} = \frac{1}{P_{\text{fring}}} = \frac{\pi}{\mu_0 w_d} \frac{1}{\ln\left(1 + \frac{\pi w_a}{2 l_g}\right)} \tag{24}$$

Fig. 8 shows the enhanced transformer magnetic equivalent model that considers the fringing effects. Fringing reluctance, as calculated in equation (24), pertains to half of the core leg; therefore, in the magnetic equivalent model, it is parallel to reluctances from two fringing reluctance gaps. The reluctances from these two fringing gaps, when parallel to the air-gap reluctance, can be represented as follows:

$$\Re_{\text{left leg}} = \Re_{\text{right leg}} = \Re_{\text{fring}} \parallel \Re_{\text{left gap}} \parallel \Re_{\text{fring}} \tag{25}$$

$$\Re_{\text{center leg}} = \Re_{\text{fring}} \parallel \Re_{\text{center gap}} \parallel \Re_{\text{fring}} \tag{26}$$

Further simplification of the magnetic equivalent model results in a single equivalent reluctance, which is defined as follows:

$$\begin{aligned} \Re_{\text{total}} = 0.5 &\left(\Re_{\text{top}} + \Re_{\text{bot}} + \Re_{\text{left leg}}\right) \\ &+ \Re_{\text{side1}} + \Re_{\text{center leg}} + 2\Re_{\text{side2}} \end{aligned} \tag{27}$$

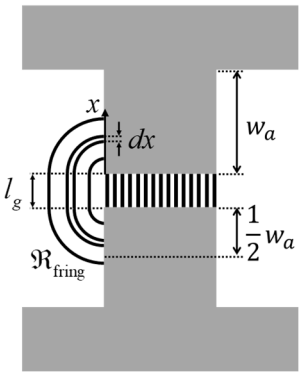

FIGURE 7. Fringing flux path model in EE core.

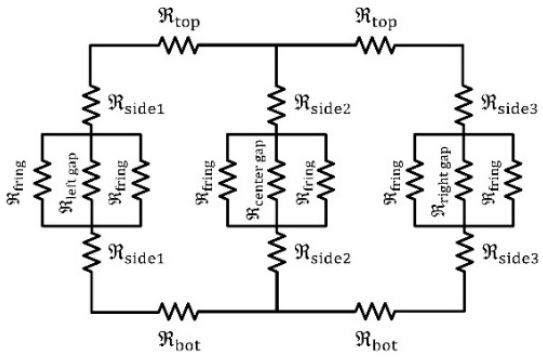

FIGURE 8. Magnetic equivalent model considering fringing effect.

V. PROPOSED TRANSFORMER DESIGN TECHNIQUE

In this section, we propose a high-frequency transformer design technique that utilizes an MOA based on the proposed magnetizing-inductance prediction model. The proposed design methodology comprises eight steps and prioritizes the minimization of the transformer volume and total loss as the primary objective functions. Further, weights are assigned to each objective function, which allows the users to arrive at an optimal design point and maintain the degree of diversity.

A. MOA

The MOA is a representative algorithm for determining the Pareto front and a set of optimal solutions that simultaneously satisfy multiple objective functions [26]. Fig. 9 shows an example of an MOA execution. The Pareto front is derived based on the utopia point and identifies the optimal region among the feasible points. The formation of the Pareto front varies based on whether the evaluated objective functions aim to minimize or maximize the values. Initially, the baseline point is determined as the point closest to the utopia point. Subsequently, a search is conducted on both the left and right sides to determine the Pareto front. This approach offers the advantage of quick execution because it starts the search from the nearest points and identifies the optimal solutions regardless of the number of iterations.

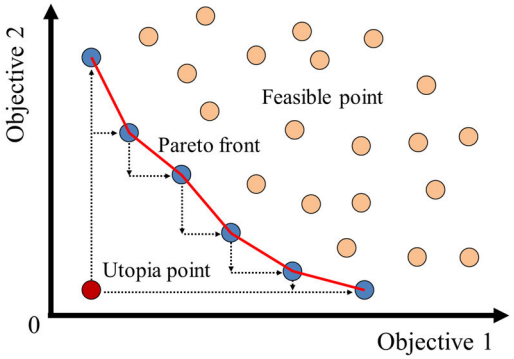

FIGURE 9. Example of using Multi-objective Optimization Algorithm (MOA).

B. TRANSFORMER DESIGN OBJECTIVE FUNCTIONS

For the objective functions required to apply the MOA, we chose the transformer volume V_t and total transformer loss P_t. The winding losses P_{winding} are calculated using equation (2), and the core losses P_{core} are evaluated using equation (5): The total transformer loss P_t and the transformer volume V_t are respectively expressed as follows:

$$P_t = P_{winding} + P_{core} \tag{28}$$

$$V_t = w_d \cdot (2w_a + 2w_b) \cdot (2w_e + 2w_s + w_c) \tag{29}$$

Subsequently, the weights were applied to derive the optimal design point from the formed Pareto front according to the preference of the user. By applying these weights, the user can select the optimal design point at which either the total transformer loss or the transformer volume is minimized.

C. TRANSFORMER DESIGN OPTIMIZATION VARIABLES

The selection of the optimization variables is critical, especially in conjunction with the choice of objective functions. Therefore, we selected independent variables specific to the transformer design as the optimization variables, the details of which are as follows:

1) Maximum flux density B_{max} (Range: 0.1 T – 0.3 T): This is determined by applying a margin to the saturation flux density B_{sat} provided by the core manufacturer.
2) Core shape: The core database in this study consisted solely of EE cores because the EE core shape was employed to apply the magnetic equivalent model proposed in Section III.
3) Core Material: The core database used in this study was composed of ferrites N87 and N97.

D. TRANSFORMER DESIGN OPTIMIZATION METHOD

The high-frequency transformer design process, which utilizes the proposed magnetic-equivalent model, comprises eight steps. Fig. 10 shows a flowchart of the proposed high-frequency transformer design.

Step 1-2: Input system parameters and desired magnetizing inductance L_m. The types of system parameters that can be input include turns ratio n_1/n_2, switching frequency f_{sw}, peak current on the primary side $I_{1,peak}$, peak current on the secondary side $I_{2,peak}$, root-mean-square (RMS) current on the primary side $I_{1,rms}$, RMS current on the secondary side $I_{2,rms}$, current density J_{max}, indow utilization factor K_u, maximum flux density B_{max}, and primary side voltage V_{pri}.

Step 3: Based on the input data, search and select an appropriate winding from the winding database. A Litz wire with a cross-sectional area greater than the calculated minimum required cross-sectional areas of the primary winding A_{w1} and secondary winding A_{w2} was selected from the winding database, considering $I_{1,rms}$, $I_{2,rms}$ and J_{max}. The cross-sectional area of the winding used for selection is given by the following:

$$A_{w1} = \frac{I_{1,rms}}{J_{max}}, A_{w2} = \frac{I_{2,rms}}{J_{max}} \tag{30}$$

Step 4-5: Using the selected winding, select a core capable of implementing the desired magnetization inductance. The core database contains cores of various sizes, and an appropriate core for the design is selected after searching through it. Once the core is selected, the number of turns on the primary side N_p, number of turns on the secondary side N_s, and air gap l_g are determined. The number of turns on the primary side N_p can be calculated using the following:

$$N_p = \frac{L_m \cdot I_{1,peak}}{A_c \cdot B_{max}} \tag{31}$$

Step 6-7: Evaluate the feasibility of the designed transformer based on specific constraints. First, we ensure that the magnetic flux density B of the designed transformer does not exceed the maximum magnetic flux density B_{max}. Second, we confirmed whether the wire fits within the selected core window area. To achieve this, we establish a wire window area factor F_w as follows:

$$F_w = \frac{N_p \cdot A_{w1} + N_s \cdot A_{w2}}{2\pi \cdot d_s \cdot w_s} \tag{32}$$

Further, we check whether the F_w of the designed transformer is below the set limit. Designs that did not satisfy these criteria were redesigned by adjusting the air gap and turn count. Scenarios in which multiple smaller cores were connected in parallel should be considered during the high-frequency transformer design process. Therefore, a core parallel limitation factor i_p was established. The design process progressed to setting the set i_p for each core. The primary turns, secondary turns, and air gaps required to achieve the target magnetizing inductance were recalculated for cores that increased in parallel. The number of cores in parallel in the core database increased incrementally by repeating the processes from Step 4 to Step 7. The design process is completed when the number of parallel cores matches the i_p factor. Then, the parameters of the designed transformer are stored in the transformer database.

Step 8: An MOA was employed to identify the optimal transformer design point within the derived transformer database. The objective functions were the transformer volume and total losses, and the design variables comprised the core attributes. Min-max normalization was used to normalize the objective functions that have different units and ranges. The normalized objective function is expressed as follows:

$$\bar{g}_i = \frac{g_i - g_{i,\min}}{g_{i,\max} - g_{i,\min}} \tag{33}$$

where g_i represents the objective function and $g_{i,max}$ and $g_{i,min}$ correspond to the maximum and minimum values of the objective function, respectively. Further, $\bar{g}_i$ denotes a normalized objective function. By applying a weighting factor η to the normalized objective function, designers can prioritize which objective functions are more crucial during the design process, thereby allowing users to adjust the relative significance of objective functions based on their desired targets and offering flexibility in the design process.

E. TRANSFORMER DESIGN IMPLEMENTATION EXAMPLE

This section presents a design example of a high-frequency transformer for an LLC resonant converter using the proposed design methodology.

Step 1-3: System parameters for the LLC resonant converter under design are input as follows: target magnetizing inductance $L_m = 20\mu$H, turn ratio $n_1/n_2 = 1.5$, resonant frequency $f_r = 300$kHz, switching frequency $f_r = 230$kHz, primary-side peak current $I_{1,peak} = 10.4$A, secondary-side peak current $I_{2,peak} = 12.5$A, primary-side RMS current $I_{1,rms} = 5$A, and secondary-side RMS current $I_{2,rms} = 8$A. The current density was $J_{max} = 3\text{A/mm}^2$, and the window utilization factor $k_u = 0.3$. The saturation flux density range B_{sat} of the ferrite core used for the transformer construction is $0.48\text{T} - 0.56\text{T}$. However, considering temperature saturation, the maximum flux density B_{max} range is selected as $0.1\text{T} - 0.3\text{T}$. Based on the input data, the required cross-sectional areas for the primary and secondary sides are $A_{1,w} = 1.66\text{Amm}^2$ and $A_{2,w} = 2.66\text{Amm}^2$, respectively. Consequently, a Litz-wire of 0.12mm/250 (2.8sq) with a cross-sectional area larger than required was selected.

Step 4-7: A core that can achieve the target magnetizing inductance of 20 μH is selected, and the transformer design is performed using the selected winding. All designs are conducted for 47 cores stored in the core database, with the core parallel limitation coefficient i_p set to 10. A redesign process is initiated if the initially designed transformer does not satisfy these constraints. If the design satisfied the constraints, it was saved in a transformer database. The accuracy of the magnetizing inductance was set to 99% and the window area coefficient F_w was limited to 0.8 (80%).

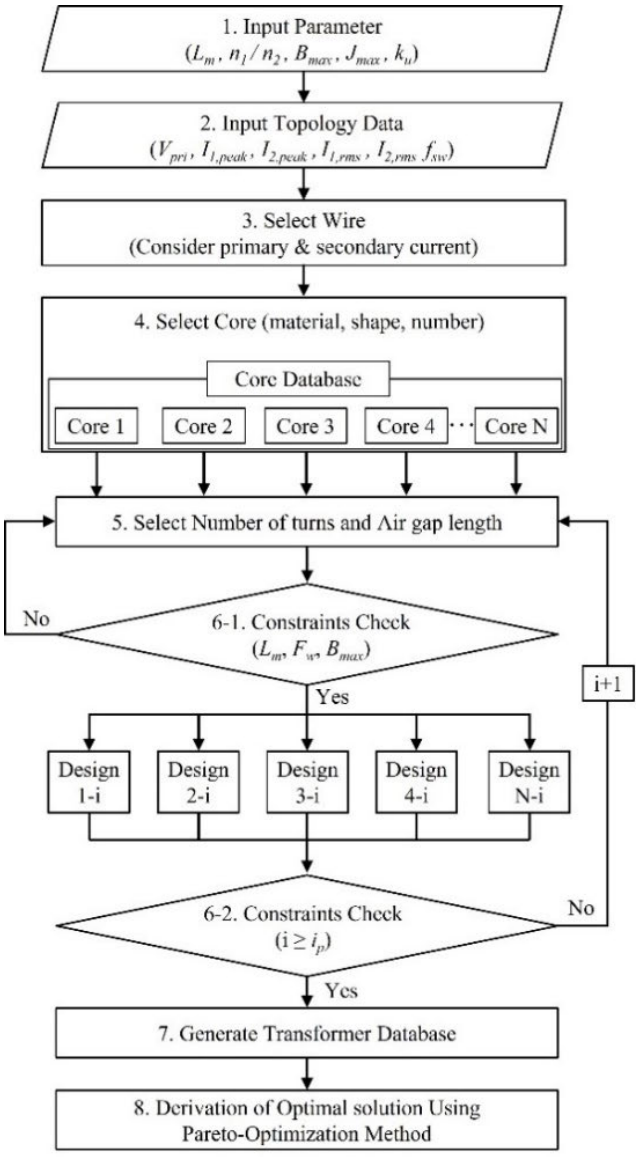

FIGURE 10. Proposed design optimization method flowchart of HFTR.

Step 8: Apply the MOA to the derived transformer database to obtain the Pareto front, which comprises the optimal transformer design points. Fig. 11 shows the normalized distribution of the transformer design points stored within the database. The Pareto front consists of 17 design points. A total of 10,000 evaluations were performed, which required 20 s for the design process. Weights were applied to select the desired design points, and the weights for the objective functions were selected as the volume weight $\eta_t = 0.75$ and loss weight $\eta_p = 0.25$, thereby deriving the optimal transformer design point. Fig. 12(a) depicts the optimal transformer design point at the selected weights, whereas Figs. 12(b) and (c) show the optimal transformer design points for different weight selections. Using this approach, versatility is ensured by allowing users to obtain various optimal transformer design points by applying different weights based on their preferences.

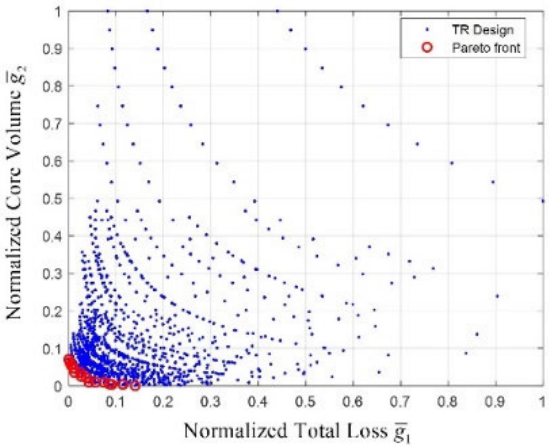

FIGURE 11. Result of Multi-objective Optimization Algorithm.

VI. VERIFICATION

A. VERIFICATION OF THE PROPOSED MAGNETIC EQUIVALENT MODEL USING EXPERIMENTAL RESULTS

Comparisons were drawn between the FEA simulations and actual measurements to validate the high prediction accuracy of the magnetic equivalent model proposed in Section IV for magnetizing inductance. An ELP 102/20/38 core is used for comparison, and the measurements are conducted by varying the air gap and number of turns. Fig. 13(a) depicts the magnetizing inductance values measured by altering the primary-side turns of the transformer from 1 to 11 turns with a 0.6 mm air gap. Conversely, Fig. 13(b) shows the magnetizing inductance values obtained by adjusting the primary-side turns of the transformer from 1 to 11 turns with a 0.8 mm air gap. The theoretical values of the conventional and proposed magnetic equivalent models, the results of the FEA simulations, and measurements from the impedance analyzer were compared. The proposed magnetic equivalent model predicts the magnetizing inductance more accurately than the conventional model.

B. VERIFICATION OF THE PROPOSED DESIGN TECHNIQUE USING EXPERIMENTAL RESULTS

The high-frequency transformer design technique is verified by fabricating and testing an actual converter. Experiments were conducted on a 500 W half-bridge LLC resonant converter. TABLE 1 lists the input parameters of the LLC resonant converter.

TABLE 2 presents the design parameters of the high-frequency transformers for LLC resonant converters derived in Chapter 4, and TABLE 3 shows the design parameters of the transformers manufactured using the method presented in Chapter 3. Additionally, Fig.14. (a) displays prototypes of high-frequency transformers manufactured based on this, alongside conventional transformers. Fig.14 (b) illustrates the volume comparison of these transformers and the efficiency comparison of LLC converters. The volume

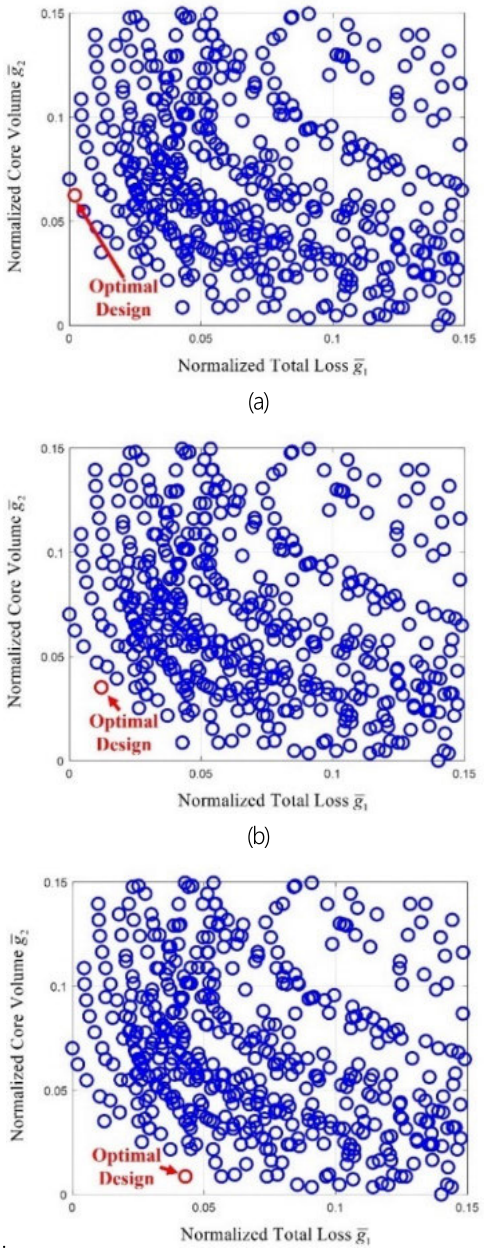

FIGURE 12. Result of deriving optimal solution at different objective function weight. (a) ηp=0.75, ηt=0.25. (b) ηp=0.5, ηt=0.5. (c) ηp=0.25, ηt=0.75.

of the high-frequency transformer prototype manufactured using the proposed design technique is 35.17cm^3, which is about 60% smaller than the 117.7cm^3 volume of transformers designed using conventional methods. The overall efficiency of the LLC converter is 94.5% when using the proposed transformer and 94.42% with the conventional transformer, showing no significant difference.

Fig. 15 shows the experimental setup for the 500 W half-bridge LLC resonant converter. A cascode GaN switch (TP65H035G4WS) was employed on the primary side, and

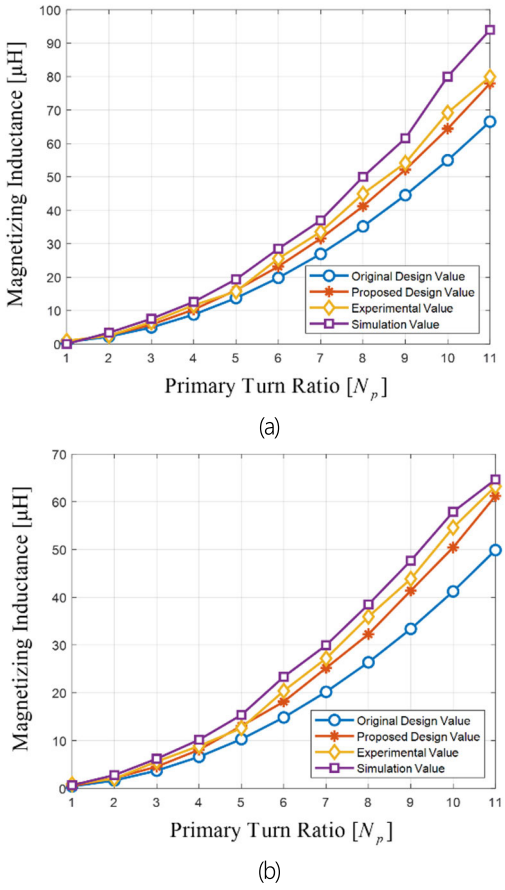

FIGURE 13. Magnetizing inductance value according to the primary turn ratio Np and air gap length lg. (a) lg=0.6mm. (b) lg=0.8mm.

a SiC diode (SCS230AE2HRC11) served as the rectification diode on the secondary side. The high-frequency transformer prototype developed using our methodology bridges the primary and secondary full-bridge rectification stages.

Fig. 16(a) shows the waveform obtained from the experiment using a transformer designed using conventional methods. By contrast, Fig. 16(b) shows the waveform obtained from our experimental setup using the proposed high-frequency transformer prototype. Both waveforms demonstrate an output voltage of 80 V from an input voltage of 180 V, with a switching frequency of 230 kHz and a load of 12.8 ohm. In both scenarios, we confirmed the correct output voltage of 80 V and verified the zero-voltage switching of the primary-side switch.

For the thermal performance, both transformers were analyzed under natural convection conditions. The theoretical temperature variation in the transformer [27] is expressed as follows:

$$\Delta T_{rise} = 450 \times \left[P_t / A_{sf} \times 10^{-4} \right]^{0.826} \tag{34}$$

where P_t represents the total loss of the transformer and A_{sf} represents the surface area of the transformer, respectively.

TABLE 1. Parameters of The LLC resonant converter.

Parameter	Value	Uint
Input voltage V_{IN}	180–240	V_{DC}
Output voltage V_{OUT}	80–120	V_{DC}
Magnetizing inductance L_m	20	μH
Resonant inductance L_r	9.4	μH
Resonant capacitance C_r	30	nF
Turn ratio N	1.5	-
Resonant frequency f_r	300	kHz

TABLE 2. Design parameters of the optimal HFTR.

Parameter	Value	Value
Core type	EE core	-
Core name	E 40/16/12	-
Number of parallel cores	2	-
Primary turn ratio N_p	9	turns
Secondary turn ratio N_s	6	turns
Air gap length l_g	0.95	mm
Volume	35.17	cm^3

TABLE 3. Design parameters of the conventional HFTR.

Parameter	Value	Value
Core type	EE core	-
Core name	E 65/32/27	-
Number of parallel cores	1	-
Primary turn ratio N_p	6	turns
Secondary turn ratio N_s	4	turns
Air gap length l_g	0.65	mm
Volume	117.7	cm^3

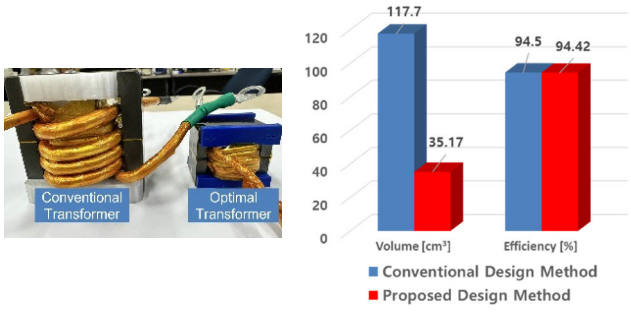

FIGURE 14. Comparison of conventional and optimal transformer. (a) Products. (b) Volume.

Fig. 17(a) shows both the theoretical and measured thermal variations obtained through experimentation for the transformer designed using conventional methods. Similarly, Fig. 17(b) presents the theoretical and measured

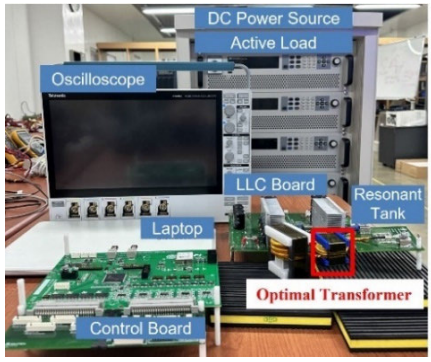

FIGURE 15. LLC resonant converter experiment setup.

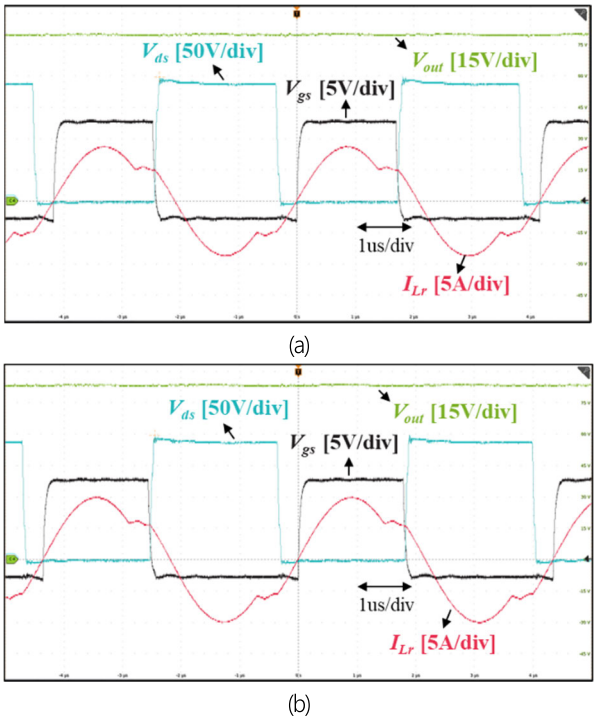

FIGURE 16. Experimental result waveform of LLC resonant converter at Vin=180V, Vout=80V. (a)conventional transformer. (b)optimal transformer.

thermal variations in the transformer prototype designed using the proposed method. Both transformers stabilized at approximately 60 °C, which is lower than the theoretical thermal prediction of 70 °C to 80 °C. The discrepancy between the calculated and experimental temperature values of the transformer can primarily arise due to inaccuracies in the transformer winding design and material properties. In the case of winding design, imprecise settings or errors in various design elements, such as the configuration of windings and the spacing between them, can lead to mismatches between the predicted and actual measured temperatures. Additionally, the material characteristics and quality of the transformer influence its thermal properties. Deviations during the manufacturing process and insufficient quality control can result in differences between experimental outcomes and

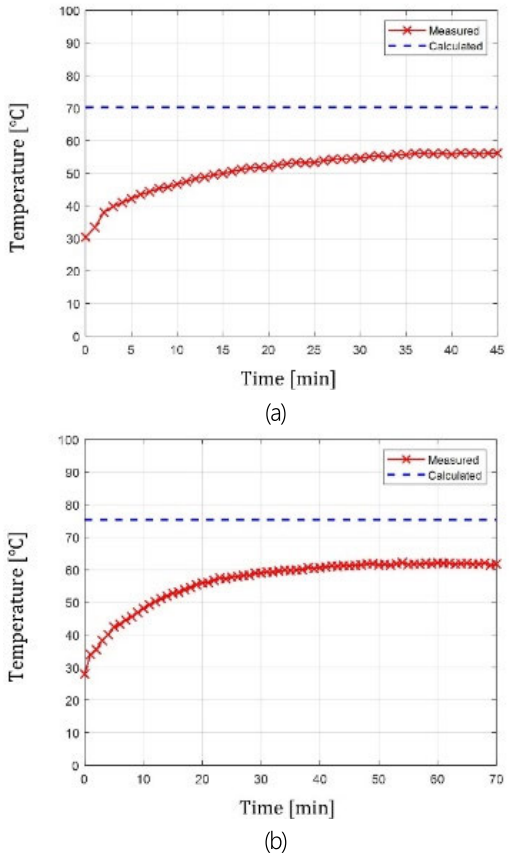

FIGURE 17. Transformer thermal performance with natural convection (a)conventional transformer (b)optimal transformer.

theoretical predictions. Therefore, in the case of Figure 17, discrepancies between the temperature of the transformer and the calculated values can occur. However, the experimental results confirm stability as the temperature remains below 70 °C.

VII. CONCLUSION

A transformer design methodology based on a magnetic equivalent model for LLC resonant converters was proposed to achieve lower magnetizing inductance error rates, and reduced design time. The magnetic equivalent model, which considers the actual path of the magnetic flux, core permeability, and fringing effect, exhibited lower magnetizing inductance error rates and a technique that applied the MOA was presented to shorten the design time. The low magnetizing-inductance error rate of the proposed magnetic equivalent model was verified through FEA element analysis simulations and actual measurements using an impedance analyzer. Finally, experiments were conducted by applying the fabricated high-frequency transformer prototype to a 500 W half-bridge LLC resonant converter. The proposed high-frequency transformer prototype demonstrated an equivalent performance compared to that of a conventional transformer manufactured with the same magnetizing inductance target. In addition, a volume reduction of approximately 60% was achieved. This result validated the effectiveness of the proposed high-frequency transformer design methodology.

REFERENCES

[1] J. Zeng, G. Zhang, S. S. Yu, B. Zhang, and Y. Zhang, "LLC resonant converter topologies and industrial applications—A review," *Chin. J. Electr. Eng.*, vol. 6, no. 3, pp. 73–84, Sep. 2020.

[2] A. Kolli, A. Gaillard, A. De Bernardinis, O. Bethoux, D. Hissel, and Z. Khatir, "A review on DC/DC converter architectures for power fuel cell applications," *Energy Convers. Manag.*, vol. 105, pp. 716–730, Nov. 2015.

[3] V. Boscaino, R. Miceli, C. Buccella, C. Cecati, H. Latafat, and K. Razi, "Fuel cell power system with LLC resonant DC/DC converter," in *Proc. IEEE Int. Electric Vehicle Conf. (IEVC)*, Florence, Italy, Dec. 2014, pp. 1–6.

[4] H. Huang, "Designing an LLC resonant half-bridge power converter," in *Proc. Texas Instrum. Power Supply Design Seminar*, 2010, pp. 1–27.

[5] R. W. Erickson and D. Maksimovic, *Fundamentals of Power Electronics*. Springer, 2020.

[6] H. C. Roters, *Electromagnetic Devices*. Hoboken, NJ, USA: Wiley, 1941, p. 246.

[7] E. S. Lee, S. H. Song, J. H. Park, and M. R. Kim, "Optimal transformer design of DAB converters in solid-state transformers for maximum power efficiency," *IET Power Electron.*, vol. 16, pp. 1625–1639, Aug. 2022.

[8] J. P. C. Smeets, L. Encica, and E. A. Lomonova, "Comparison of winding topologies in a pot core rotating transformer," in *Proc. 12th Int. Conf. Optim. Electr. Electron. Equip.*, Brasov, Romania, May 2010, pp. 103–110.

[9] M. Sippola and R. E. Sepponen, "Accurate prediction of high-frequency power-transformer losses and temperature rise," *IEEE Trans. Power Electron.*, vol. 17, no. 5, pp. 835–847, Sep. 2002.

[10] E. L. Barrios, A. Ursua, L. Marroyo, and P. Sanchis, "Analytical design methodology for Litz-wired high-frequency power transformers," *IEEE Trans. Ind. Electron.*, vol. 62, no. 4, pp. 2103–2113, Apr. 2015.

[11] P. C. Sarker, Md. R. Islam, Y. Guo, J. Zhu, and H. Y. Lu, "State-of-the-art technologies for development of high frequency transformers with advanced magnetic materials," *IEEE Trans. Appl. Supercond.*, vol. 29, no. 2, pp. 1–11, Mar. 2019.

[12] J. Cale, S. D. Sudhoff, and L.-Q. Tan, "Accurately modeling EI core inductors using a high-fidelity magnetic equivalent circuit approach," *IEEE Trans. Magn.*, vol. 42, no. 1, pp. 40–46, Jan. 2006.

[13] M. A. Batdorff and J. H. Lumkes, "High-fidelity magnetic equivalent circuit model for an axisymmetric electromagnetic actuator," *IEEE Trans. Magn.*, vol. 45, no. 8, pp. 3064–3072, Aug. 2009.

[14] A. Garcia-Bediaga, I. Villar, A. Rujas, L. Mir, and A. Rufer, "Multiobjective optimization of medium-frequency transformers for isolated soft-switching converters using a genetic algorithm," *IEEE Trans. Power Electron.*, vol. 32, no. 4, pp. 2995–3006, Apr. 2017.

[15] D. Ahmed, L. Wang, Z. Dai, and M. Wu, "Pareto-optimal design of Litz-wire gapped-core high-frequency transformer for LLC converters," *IEEE Trans. Ind. Electron.*, vol. 69, no. 9, pp. 8883–8894, Sep. 2022.

[16] I. Villar, U. Viscarret, I. Etxeberria-Otadui, and A. Rufer, "Global loss evaluation methods for nonsinusoidally fed medium-frequency power transformers," *IEEE Trans. Ind. Electron.*, vol. 56, no. 10, pp. 4132–4140, Oct. 2009.

[17] D. C. Jiles and D. L. Atherton, "Theory of ferromagnetic hysteresis," *J. Magn. Magn. Mater.*, vol. 61, nos. 1–2, pp. 48–60, Sep. 1986.

[18] F. Preisach, "Über die magnetische nachwirkung," *Zeitschrift für Physik*, vol. 94, nos. 5–6, pp. 277–302, May 1935.

[19] G. Bertotti, "General properties of power losses in soft ferromagnetic materials," *IEEE Trans. Magn.*, vol. 24, no. 1, pp. 621–630, Jan. 1988.

[20] W. A. Roshen, "A practical, accurate and very general core loss model for nonsinusoidal waveforms," *IEEE Trans. Power Electron.*, vol. 22, no. 1, pp. 30–40, Jan. 2007.

[21] K. Venkatachalam, C. R. Sullivan, T. Abdallah, and H. Tacca, "Accurate prediction of ferrite core loss with nonsinusoidal waveforms using only Steinmetz parameters," in *Proc. IEEE Workshop Comput. Power Electron.*, Mayaguez, PR, USA, Jun. 2002, pp. 36–41.

[22] A. Van den Bossche, V. C. Valchev, and G. B. Georgiev, "Measurement and loss model of ferrites with non-sinusoidal waveforms," in *Proc. IEEE 35th Annu. Power Electron. Specialists Conf.*, Aachen, Germany, Jun. 2004, pp. 4814–4818.
[23] A. Balakrishnan, W. T. Joines, and T. G. Wilson, "Air-gap reluctance and inductance calculations for magnetic circuits using a Schwarz–Christoffel transformation," *IEEE Trans. Power Electron.*, vol. 12, no. 4, pp. 654–663, Jul. 1997.
[24] A. Lotfi and E. Rahimpour, "Optimum design of core blocks and analyzing the fringing effect in shunt reactors with distributed gapped-core," *Electric Power Syst. Res.*, vol. 101, pp. 63–70, Aug. 2013.
[25] S.-J. Kim, W.-Y. Kim, J.-M. Lee, and Y.-C. Bae, "Modeling of flux leakage in a magnetic circuit with permanent magnet," *Trans. Korean Soc. Noise Vibrat. Eng.*, vol. 21, no. 2, pp. 99–105, Feb. 2011.
[26] M. J. Reddy and D. N. Kumar, "Multi-objective optimization using evolutionary algorithm," *Water Resour. Manag.*, vol. 20, pp. 861–878, 2006.
[27] C. W. T. McLyman, *Transformer and Inductor Design Handbook*, 4th ed. New York, NY, USA: CRC Press, 2011.

HAE-CHAN PARK received the B.S. and M.S. degrees in electrical engineering from the Korea National University of Transportation, Chungju, South Korea, in 2017. He is currently pursuing the Ph.D. degree with the Energy Power Electronics Control System Laboratory, Hanyang University, Seoul, South Korea. His research interests include the protection and application of wide-bandgap devices and inductive power transfer and the design of high-density and high-efficiency power converters.

JONG-UK YANG received the B.S. degree in electronic engineering from Hanyang University, Ansan, South Korea, in 2021, and the M.S. degree in electrical engineering from Hanyang University, Seoul, South Korea, in 2023.

In 2023, he joined LG Electronics, Seoul, a home appliance and air solution company, where he is currently a Professional Research Engineer with the Power Electronics Research and Development Laboratory. His current research interests include control technology for electric machines and power conversion circuits.

JIN-SU JANG received the B.S. degree in electrical engineering from Konkuk University, Seoul, Republic of Korea, in 2006, and the M.S. degree in electrical engineering from Hanyang University, Seoul, in 2009, where he is currently pursuing the Ph.D. degree in electrical engineering with the Energy Power Electronics Control System Laboratory. His research interests include high-density and high-efficiency power conversion systems.

RAE-YOUNG KIM (Senior Member, IEEE) received the B.S. and M.S. degrees in electrical engineering from Hanyang University, Seoul, South Korea, in 1997 and 1999, respectively, and the Ph.D. degree in electrical engineering from Virginia Polytechnic Institute and State University, Blacksburg, VA, USA, in 2009.

From 1999 to 2004, he was a Senior Researcher with the Hyosung Heavy Industry Research and Development Center, Seoul. In 2009, he was a Postdoctoral Researcher with National Semiconductor Corporation, Santa Clara, CA, USA, involved in a smart home energy management system. Since 2010, he has been with Hanyang University, where he is currently a Professor with the Department of Electrical and Biomedical Engineering. In 2016, he was a Visiting Scholar with the Center for Power Electronics Systems (CPES), Virginia Polytechnic Institute and State University. His research interests include the design of high-power density converters and the distributed control of power converters for modular power converter systems in applications of renewable energy, wireless power transfer, microgrids, and motor drives.

Dr. Kim was a recipient of the 2007 First Prize Paper Award from the IEEE Industry Applications Society (IAS).